

Chapter 2

Surface Structures and the Crystal Habit of Growing Particles

Abstract A truncated single-crystal surface varies to a more stable two-dimensional array of atoms by raising the temperature. On the other hand, metal particles may grow via a two-dimensional precursor array of atoms. The (1×1) Au(111), Au(110), and Au(100) surfaces undergo reconstruction in electrolyte solutions at a certain negative electrode potential (vs. SCE). The icosahedral or decahedral Au particles are preferentially grown on an electrode held at the same negative electrode potential making reconstruction of Au crystal surfaces. The result suggests that metal particles may grow via precursor states of metal array which are similar to two-dimensional array of the reconstructed surfaces. Multi-twin Pt particles are also formed at highly negative electrode potential.

Keywords Reconstruction of metal surfaces • Pt(100) • Au(111) • Au(100) • Au(110) • Si(111) • Electrode potential • Multi-twin metal particles • Potential-induced surface reconstruction • Quasi-compounds • UPD (under-potential deposition) • Cu–Au alloy particles formed by UPD

A (1×1) -Pt(100) surface is stabilized by forming a hexagonal (5×20) -Pt(100) surface, and a (1×1) -Si(111) surface is reconstructed to a (7×7) -Si(111) surface. The reconstructed surface is directly observed by the scanning tunneling microscopy (STM) as shown in Fig. 2.1a and b [1]. In the case of a truncated (1×1) -Si(111) surface, every Si-atom has one unsaturated covalent bond called a “dangling bond,” the surface is stabilized by lowering the number of Si atoms with a dangling bond in vacuum at ca. 1200 K, and a characteristic (7×7) -Si(111) surface is formed.

If atoms or molecules are adsorbed on a stabilized surface, the surface may undergo additional reconstruction, the so-called adsorption-induced reconstruction, whereby the total energy including the adsorption energy is lowered by the reconstruction. The reverse reconstruction from a stabilized (5×20) -Pt(100) clean surface to a metastable (1×1) -Pt(100) surface is attainable by using adsorption of CO and O₂ [1]. That is, the heat of adsorption of O₂ on the (1×1) -Pt(100) surface is higher than that on the hex- (5×20) -Pt(100) surface, which is the driving force

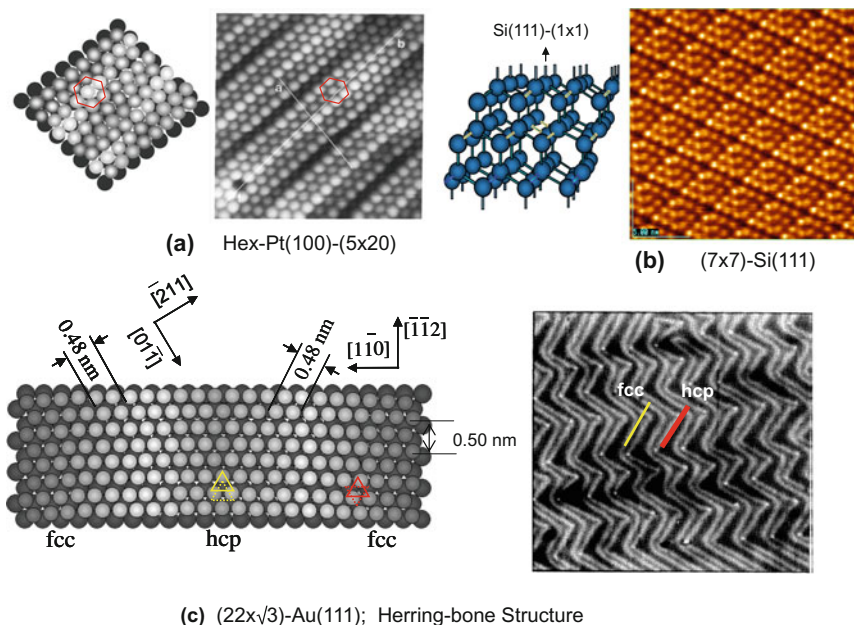


Fig. 2.1 Typical examples of the surface taking a 2-D stabilized conformation: **a** hex-(5 × 20)Pt (100) surface [1], **b** (7 × 7)-Si(111) surface, and **c** (22 × √3)-Au(111) surface, named herringbone structure, formed by alternated stacking of hcp and fcc regions, with bright ridge lines appearing between them, as shown by a model of (22 × √3)-Au(111) [3]

for the reverse reconstruction from (5 × 20)-Pt(100) to a metastable (1 × 1)-Pt (100) surface. By this process, a metastable (1 × 1)-Pt(100) surface is attainable by removing the adsorbed oxygen by reacting with H₂ at low temperature.

Reconstruction of the Au(111) surface is another interesting example, induced by anisotropic shortening of the lattice distance in the topmost layer. In this case, an anisotropic shortening of ~ 4.2% of the Au–Au lattice distance, from 0.50 to 0.48 nm, occurs in the topmost layer along the $\langle 2\ 1\ 1 \rangle$ direction on the (1 × 1)-Au (111) plane. As a result, the Au atoms in the topmost layer make an array of ABC/ABC (fcc structure) areas and AB/AB (hcp structure) stacking areas separated by ridges of atoms. Figure 2.1c shows an STM image of a reconstructed Au(111) surface, the so-called herringbone (22 × √3)-Au(111) surface, where the wider dark stripe corresponds to a fcc stacking area, the narrow dark stripe corresponds to a hcp stacking area, and the bright line between them is a ridge of Au atoms (the (1 × 1)-Au(111) surface has three equivalent axes) [3]. The Au–Au distance of the reconstructed (22 × √3)-Au(111) structure is reduced from the bulk distance of 0.50 to 0.48 nm along the $\langle 1\bar{1}\ 0 \rangle$ axis, which is a ca. 4.2% reduction in the Au–Au distance. As a result, a (22 × √3)-Au(111) surface with the slightly distorted chevron or “herringbone” pattern shown in Fig. 2.1c is formed. The (22 × √3)-Au (111) surface is energetically inhomogeneous due to lattice strain, which influences

the preferential growth of nanoparticles of Au [2], Co [3], Fe [4], Ni [5], and Ag [6] at the elbow sites on the $(22 \times \sqrt{3})$ -Au(111) surface.

Another notable feature of the Au(111) surface is a reversible reconstruction in aqueous solution that can be induced by an electrochemical potential. The potential-induced reconstruction of the Au surface was first suggested by Hamelin [7] to explain the hysteresis of the electro-capacitance curve of an Au(111) surface, and the reconstruction was confirmed by Kolb et al. by using LEED [8]. A (1×1) -Au(111) surface changes to a $(22 \times \sqrt{3})$ structure when it is biased at a certain negative electrochemical potential relative to the saturated calomel electrode (SCE) in an electrolyte solution, which is similar to the reconstruction taking place in vacuum on raising temperature. It is notable that Au(111), Au(100), and Au(110) surfaces all undergo reconstruction at an equally negative potential, but the electrochemical potential for the reverse reconstruction to the (1×1) surface depends on the crystal plane, $\text{Au}(110) < \text{Au}(100) < \text{Au}(111)$, depending on the density of Au atoms, as shown in Fig. 2.2a [9, 10]. This result suggests that the array of the topmost Au atoms depends on the electrochemical potential in aqueous solution. If the structure of the two-dimensional array of Au atoms depends on the

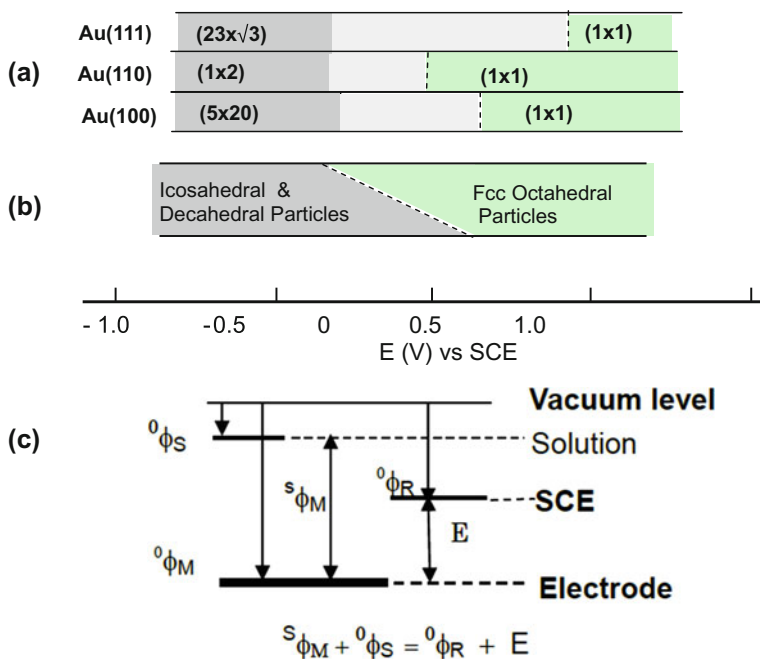


Fig. 2.2 **a** Stable surface structures of Au(111), Au(110), and Au(100) depending on the electrochemical potential (E) with respect to SCE in 0.1 M HClO_4 solution. **b** Au particles grown on a C-coated-Au-mesh electrode in 50 mM HClO_4 + 1 mM HAuCl_4 solution. Crystal habit of Au particles depends on the electrochemical potentials [11]. **c** Relative potential levels of an electrode (ϕ_M) in an electrolyte solution with respect to the SCE and the Fermi level in the vacuum

electrochemical potential, the growth of Au particles from Au^{3+} ions on an electrode may be influenced by the electrode potential, which would be the array of Au atoms in a precursor state of the growth of a crystal. If this is the case, the electrode potential will give some effect on the growing form of crystals. As predicted, multi-twin Au particles grow on a carbon-coated Au gauze held at the electrochemical potential inducing the reconstruction of Au(111), Au(100), and Au(110) surfaces as shown in Fig. 2.2b [11, 12]. A more interesting fact is that a similar potential effect is observed not only on Au particles but also on most fcc metal particles, although potential-induced surface reconstructions have been reported only on Au surfaces.

If we consider the electrode potential (${}^0\phi_{\text{M}}$) from the vacuum level, it is given by the equation: ${}^0\phi_{\text{M}} = {}^s\phi_{\text{M}} + {}^0\phi_{\text{s}} = {}^0\phi_{\text{R}} + E$ as illustrated in Fig. 2.2c, where the electrode potential E (V) is referred to SCE (the standard saturated calomel electrode). If the Fermi level of the electrolyte solution (${}^0\phi_{\text{s}}$) can be presumed to be in the range of 0.1 ~ 0.2 V [13], one can estimate the electrode level (${}^0\phi_{\text{M}}$) to the potential level of the SCE (${}^0\phi_{\text{R}}$) from the vacuum. By the shift of the vibrational frequency of adsorbed CO on a Pt(111) electrode as a function of the electrostatic potential, one can evaluate the Fermi level of the metal in solution compared to that in vacuum. When the electrode potential is held at the zero-charge (E_{zc}) potential, the stretching vibrational frequency of adsorbed CO on the Pt electrode becomes equal to that of adsorbed CO on Pt(111) in vacuum [14]. Taking these results into account, the Fermi level of an electrode (${}^0\phi_{\text{M}}$) from the vacuum level relative to SCE (E) is schematically shown in Fig. 2.2c. As shown in Fig. 2.2b, when an electrode is held at a negative potential with respect to SCE, the fractions of decahedral and icosahedral Au particles increase with decreasing (more negative) potential.

The left-hand-side TEM image shown in Fig. 2.3a shows an ordinary octahedral Au crystal particle formed at +0.33 V and its electron diffraction pattern along the $\langle 100 \rangle$ direction, and the other two TEM images of Au crystal particles are formed at -0.30 and -0.55 V, respectively [11, 12]. The fractions of Au crystal particles formed on an Au-mesh electrode in a HAuCl_4 (1×10^{-3} M) + HClO_4 (0.5 M) solution at potentials ranging from 0.35 to -0.55 V (SCE) are shown in Fig. 2.3b. It is known that the shape of Au crystal particles is clearly affected by the electrochemical potential as shown by the TEM image, and the decahedral Au particles formed at -0.30 V and icosahedral Au particles at -0.55 V are shown in Fig. 2.3a. The ratio of multi-twin particles to the total particles per mm^2 (B/A) linearly increases with respect to the negative electrode potential as shown in Fig. 2.3b, and more than 60 % of Au particles were either icosahedral or decahedral, with the decahedral Au particles being preferred.

Potential-induced surface reconstruction of the Au(111) surface is caused by an anisotropic shortening of the Au–Au distance in 4–5 %, and radially shaped nanometer-sized Au particles resulted from the growth of multiply twinned particles [15]. Formation of multi-twin Au particles, as well as decahedral and icosahedral Au particles, was first observed by Ino and Ogawa [16] on a heated NaCl crystal plane in vacuum and also observed on a heated graphite surface by Wayman and

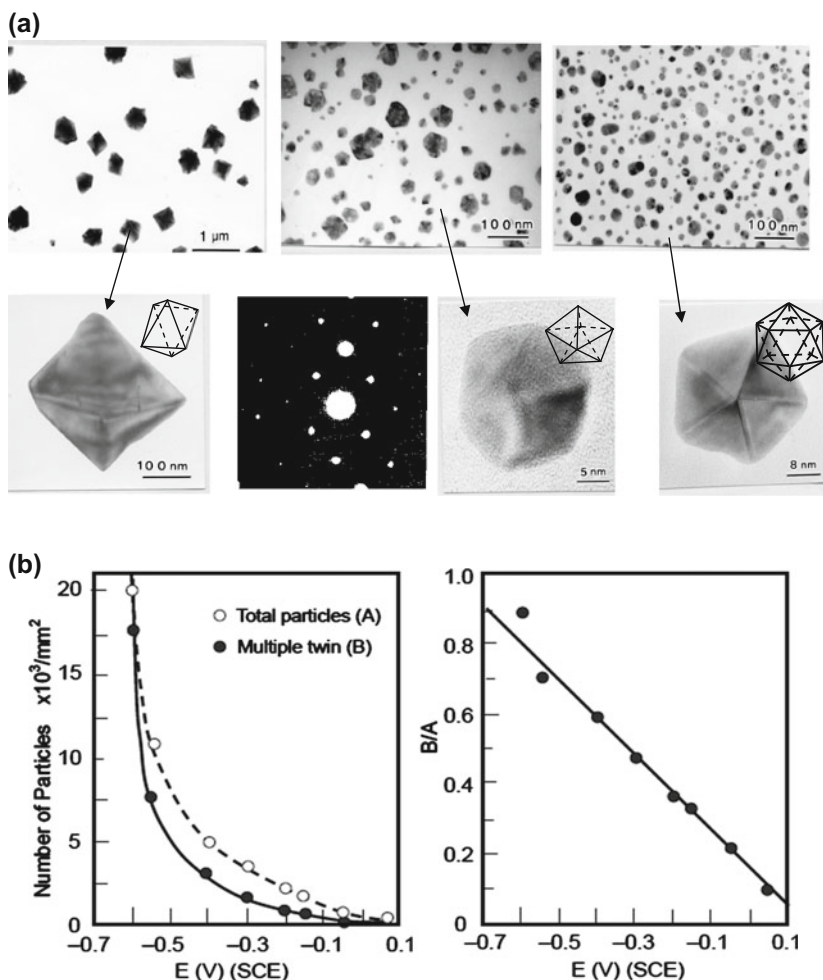


Fig. 2.3 **a** TEM images of octahedral Au particles grown at +0.33 V, and of decahedral and icosahedral Au particles attained at -0.30, and -0.55 V [11]. Electron diffraction pattern along the $\langle 100 \rangle$ direction of the fcc octahedral Au particles grown at 0.35 V. **b** Total number of Au particles (A) per mm² (○) formed in 60 s, and the number of decahedral and icosahedral multi-twin particles (B) (●) depending on the potential (E). The B/A ratio shows preferential growth of multi-twin particles (B) at negative electrochemical potentials [12]

Darby [17]. The decahedral and icosahedral Au particles were explained as resulting from the aggregation of five and twenty twin particles. Taking these results into account, the total surface energy of particles is lowered by forming twin boundaries, which is the driving force for the growth of icosahedral or decahedral multi-twin Au particles.

The reconstructed structure is released by keeping the Au surface at a positive potential (SCE) in solution, and the (1×1) surface is recovered. However, the icosahedral and decahedral Au particles cannot be changed to octahedral fcc particles by holding them at the corresponding positive potentials in solution. In other words, the two-dimensional array of Au atoms is reversible depending on the electrochemical potential, but once formed, bulk structure of Au particles cannot be reformed by the change in surface structure. It should be pointed out that potential-induced surface reconstruction has not been observed on other than Au surfaces, but the growth of decahedral and icosahedral particles was observed for Cu, Ni, Pd, and Ag particles at negative electrode potential (SCE) [18]. Pt is a highly stable metal giving no bulk phase reconstruction, but decahedral and/or icosahedral Pt particles were formed at -0.9 V (SCE) in a solution of 0.05 M $\text{CsClO}_4 + 1$ mM PtCl_4 at -0.5 V, where neither Cl^- nor ClO_4^- ions were adsorbed on the Pt surface [19]. These results might reflect the array of metal atoms in the precursor state of nano-sized metal particles growing in solution under the electrostatic field.

As is known, the electrochemical self-deposition of metal ions occurs at the Nernst equilibrium potential (E_r), but no electrochemical deposition proceeds at potentials more positive than the reversible Nernst equilibrium potential E_r . However, the deposition of foreign metal atoms occurs at potentials more positive than the Nernst self-deposition potential, which is known as the under-potential deposition (UPD) of foreign metal atoms. Figure 2.4 shows the under-potential deposition (UPD) of Cu^{2+} ions on a Au(111) surface in a H_2SO_4 solution given by Kolb et al. [20]. A $(\sqrt{3} \times \sqrt{3})\text{R}30$ structure is adopted on the Au(111) surface with UPD-deposited Cu^+ ions, and it changes to a (1×1) structure on deposition of Cu^0 as illustrated in Fig. 2.4. In essence, UPD of Cu^{2+} ions creates a $2/3$ monolayer of Cu^+ ions on the Au(111) surface, and one monolayer deposition of Cu^0 is formed at the lower electrode potential [21, 22]. Manne et al. [23] studied a stripped-down electrodeposited Cu layer on a Au(111) surface at an UPD potential in different electrolytes by atomic force microscopy (AFM), showed that the UPD monolayer formed different structures in different electrolytes, and showed that the deposited Cu atoms on Au(111) surface adopt a close-packed array with a spacing of 0.29 nm in a perchloric acid electrolyte solution, but take on a more open lattice spacing of 0.49 nm in a sulfate electrolyte.

When a carbon-coated Au-mesh electrode (C-coated Au) is held at the Nernst potential of Au^{3+} ion in a solution of $(\text{Au}^{3+} + \text{Cu}^{2+})$ ions, Au particles are formed, but no growth of individual Cu^0 particles occurs. However, the UPD of Cu^{2+} ions creates a Cu^+ or Cu^0 layer on the Au particles formed on the C-coated electrode; that is, Au^{3+} and Cu^{2+} ions are alternately deposited one after the other at the UPD potential of the Cu^{2+} ion. The composition of Cu/Au UPD particles formed on an Au-mesh electrode in a solution of 1 mM $\text{HAuCl}_4 + 0.1$ M $\text{HClO}_4 + \xi$ M $\text{Cu}(\text{ClO}_4)_2$ ($\xi = 0.10$ M ~ 0.001 M) varies depending on the concentration of Cu^{2+} ions and electrode potential as shown in Fig. 2.5b, and the Cu/Au ratio of alloy particles extrapolated to $(E - E_r \approx 0)$ in Fig. 2.5b suggests the formation of 50 % Cu and 50 % Au alloy particles [12, 24–27]. The results are in good agreement with

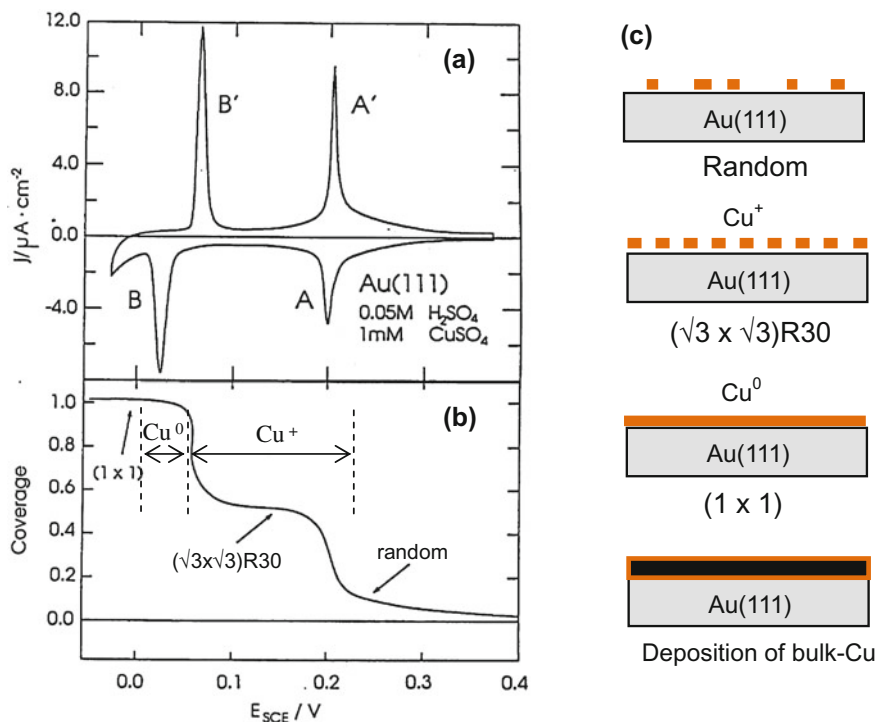


Fig. 2.4 Under-potential deposition (UPD) of Cu^{2+} ion on a Au(111) surface. **a** Cyclic current–potential curve (1 mV/sec) showing under-potential deposition (UPD) of Cu^{2+} ions on an Au(111) surface in 0.05 M H_2SO_4 + 1 mM CuSO_4 . **b** The structure of Au(111) surface changed by the deposition of Cu^+ and Cu^0 , where the coverage was derived from the charge of UPD Cu ions [20]. **c** Illustration of the deposited of Cu^+ and Cu^0 on the Au(111) surface

the UPD mechanism for the formation of Cu–Au alloy particles as one monolayer Cu^0 deposits on the Au(111) surface, as shown in Fig. 2.4.

When the electrode potential is held at higher than the UPD potential E_r ($E - E_r > 0$), the deposition rate of Au^{3+} ions to Au^0 is increased with increasing potential, whereas the UPD rate of Cu^{2+} ions may remain at a constant rate, so that the fraction of Au in the Cu–Au particles increases with electrode potential in a 1 mM Au^{3+} ion solution. It is a noteworthy result that the Cu/Au ratio maintains a constant value over a wide concentration range of Cu^{2+} ions (0.1–0.001 M) at potentials more positive than the Nernst potential of Au^{3+} ion ($E - E_r \approx 0$). The layer-by-layer deposition of Au^{3+} and Cu^{2+} ions forming Cu–Au alloy was confirmed by the Debye–Scherrer rings as shown in Fig. 2.5a, where the lattice of the Cu–Au alloy (Cu 30 %) particles was shortened compared to that of Au. If the experiment is performed at lower than the Nernst equilibrium potential of Cu^{2+} ion ($E < E_r$), the deposition rate of Cu depends on the concentration of Cu^{2+} ion, so that

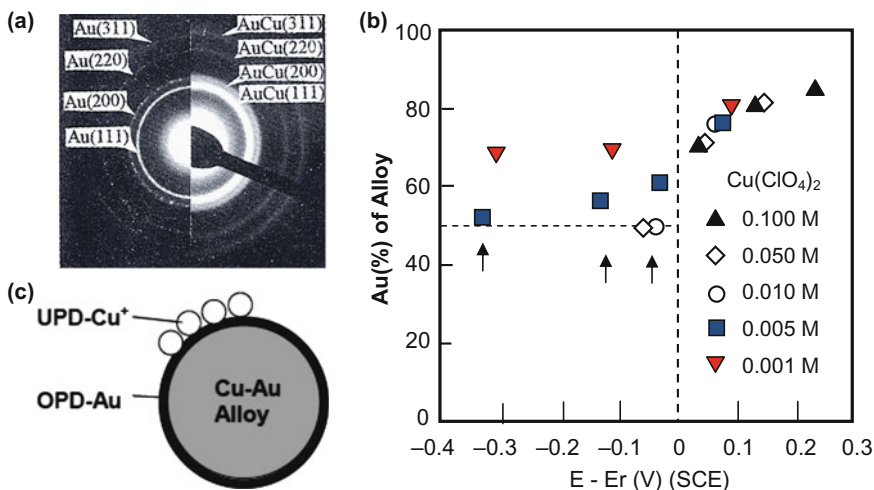


Fig. 2.5 Formation of Cu–Au alloy particles by simultaneous electrochemical deposition of Cu^{2+} and Au^{3+} ions in the UPD region of Cu^{2+} deposition on Au particles. **a** Debye–Scherrer ring of Au particles (*left*) prepared in 1 mM HAuCl_4 + 0.1 M HClO_4 at -0.5 V (SCE) and of Cu–Au alloy particles (Cu 30 %) formed in 1 mM HAuCl_4 + 0.1 M HClO_4 + 50 mM $\text{Cu}(\text{ClO}_4)_2$ at 0.1 V (SCE). **b** Au (%) in Cu–Au alloy particles depending on the electrode potential in a solution 1 mM HAuCl_4 + 0.1 M HClO_4 + ξ M $\text{Cu}(\text{ClO}_4)_2$, where the concentration of Cu^{2+} ion (ξ) was changed from 0.1 M to 0.001 M. E_r is the reversible Nernst potential of Cu^{2+} ion. Arrows indicate the potential for simultaneous formation of Cu_2O . **c** A model of UPD of Cu^+ on an OPD Au layer, which changes to a Cu–Au alloy particle [24]

the composition of the Cu–Au alloy particles depends on the concentration of Cu^{2+} ion in solution, as shown with the arrows in Fig. 2.5b. It is notable that Cu–Au alloy particles also form multi-twin particles, although the UPD of Cu^{2+} ion on Au particles occurs at a potential more positive than that required for the potential-induced reconstruction of Au surfaces, and also more positive than the formation potential of the decahedral and icosahedral multi-twin Au particles shown in Fig. 2.2a and b [18, 24, 28, 29]. This result may indicate that the shortening of the lattice distance by forming a Cu–Au surface alloy is responsible for the formation of multi-twin Cu–Au alloy particles.

References

1. A. Borg, A.-M. Hilmen, and E. Bergene, *Surf. Sci.*, 306 (1994) 10.
2. C.A. Lang, M.M. Dovek, J. Nogami, and C.F. Quate, *Surf. Sci.*, 224 (1989) L947.
3. B. Voigtländer, G. Meyer, and N.M. Amer, *Phys. Rev. B* 44 (1991) 10354.
4. B. Voigtländer, G. Meyer, and N.M. Amer, *Surf. Sci. Lett.* 255 (1991) L529.
5. D.D. Chambliss, R.J. Wilson, and S. Chang, *Phys. Rev. Lett.* 66 (1991) 1721.
6. D.D. Chambliss and R.J. Wilson, *J. Vac. Sci. Technol. B* 9 (1991) 928.

7. A. Hamelin, *J. Electroanal. Chem.*, 142 **(1982)** 299.
8. M.D. Kolb, G. Lehmpfuhl, and M.S. Zei, *J. Electroanal. Chem.*, 179 **(1984)** 289.
9. A. Hamelin, X. Gao, M.J. Weaver, *J. Electroanal. Chem.*, 323 **(1992)** 361.
10. X. Gao and M.J. Weaver, *Surf. Sci.* 313 **(1994)** L 775.
11. D-L. Lu, Y. Okawa, K. Suzuki, and K-I. Tanaka, *Surf. Sci.*, 325 **(1995)** L397.
12. D-L. Lu, Y. Okawa, M. Ichihara, A. Aramata, and K-I. Tanaka, *J. Electroanal. Chem.*, 406 **(1996)** 101.
13. S. Trasatti, *J. Electroanal. Chem.* 150 **(1983)** 1.
14. S-C. Chang, X. Xiang, J.D. Roth, and M.J. Weaver, *J. Phys. Chem.*, 95 **(1991)** 5378.
15. P-Y. Gao, W. Kunath, H. Gleiter, and K. Weiss, *Z. Phys. D* 12 **(1989)** 119.
16. S. Ino, *J. Phys. Soc. Jpn*, 21 **(1966)** 346; S. Ino and S. Ogawa, *J. Phys. Soc. Jpn*, 22 **(1967)** 1365.
17. C.M. Wayman and T.P. Darby, *J. Cryst. Growth*, 28 **(1975)** 55.
18. D-L. Lu and K-I. Tanaka, *J. Phys. Chem. B* 101 **(1997)** 4030.
19. D-L. Lu, K-I. Tanaka, *Surf. Sci.*, 373 **(1997)** L339.
20. M.H. Holzle, U. Retter and D.M Kolb, *J. Electroanal. Chem.*, 364 **(1994)** 286.
21. D.M. Kolb, *Adv. Electrochem.*, 11 **(1978)** 125.
22. I.H. Omar, H.J. Pauling, K. Juttner, *J. Electrochem. Soc.*, 140 **(1993)** 2187.
23. S. Manne, P.K. Hansma, J. Massie, V.B. Elings, A.A. Gewirth, *Science*, 251 **(1991)** 183.
24. D-L. Lu and K-I. Tanaka, *J. Electroanal. Chem.*, 430 **(1997)** 69.
25. D-L. and K-I. Tanaka *J. Solid Electrochem.* 1 **(1997)** 187.
26. D-L. Lu and K-I. Tanaka, *Surf. Sci.*, 409 **(1998)** 283.
27. D-L. Lu and K-I. Tanaka, *J. Electrochem. Soc.*, 143 **(1996)** 2105.
28. D-L. Lu and K-I. Tanaka, *Langmuir*, 18 **(2002)** 3226.
29. D-L. Lu and K-I. Tanaka, *Phys. Rev. B* 55 **(1997)** 13865.

Dynamic Chemical Processes on Solid Surfaces

Chemical Reactions and Catalysis

Tanaka, K.-i.

2017, X, 192 p. 95 illus., 74 illus. in color., Hardcover

ISBN: 978-981-10-2838-0